Electrical conductivity increase by order of magnitude through controlling sintering to tune hierarchical structure of oxide ceramics

Sergio A. Paredes-Navia, Liang Liang, Cesar-Octavio Romo-De-La-Cruz, Ellena Gemmen, Andre Fernandes, Jacky Prucz, Yun Chen, Xueyan Song [*]

Department of Mechanical and Aerospace Engineering, West Virginia University, Morgantown, WV, 26506, USA

A B S T R A C T

Perovskite calcium manganate $CaMnO_{3-\delta}$ is representative of an essential group of semiconductors with unique physical phenomena including colossal magnetoresistance and thermoelectric properties. For the large-scale applications that require the utilization of oxide ceramics, the polycrystalline materials' physical properties such as conductivity can be controlled and ultimately optimized through tuning the ceramics sintering conditions. In the present study, the impact of the sintering temperature on the structure and thermoelectric performance of $CaMnO_{3-\delta}$ is systematically studied. For the ceramics pellets made of precursors powders synthesized using the chemical sol-gel reaction, the increase in the sintering temperature dramatically increases the electrical conductivity by order of magnitude and simultaneously increases the Seebeck coefficient. Meanwhile, the thermal conductivity increases with the rise of the sintering temperature. Among the samples sintered at different temperatures, the peaking thermoelectric Figure of Merit *ZT* of pristine $CaMnO_{3-\delta}$ reached 0.28, which is a factor of 2.5 higher than the highest reported *ZT* for pristine $CaMnO_{3-\delta}$ and approached that of the doped single-phase $CaMnO_{3-\delta}$. The electrical and thermal properties changes were interpreted based on the oxide ceramics hierarchical structure evolutions, from unit cell level to micron scales, induced by changes of sintering temperatures.

1. Introduction

Perovskite calcium manganate [1,2] $CaMnO_{3-\delta}$ has been firstly synthesized in the 1960's and studied since then due to their unique magnetic properties such as colossal magnetoresistance, for which the electrical resistivity decrease after applying a magnetic field near the magnetic ordering Curie temperature [3,4]. In 1995, the research interest of the $CaMnO_{3-\delta}$ further merged due to the discovery of its thermoelectric [2] properties or its ability to convert the temperature difference into electricity or vice versa. As the n-type semiconductor, $CaMnO_{3-\delta}$ could be paired with a p-type thermoelectric oxide such as $Ca_3Co_4O_9$ [5,6] and form thermoelectric unicouple and modules. Such thermoelectric devices are without moving parts and free maintenance for solid-state power generation or cooling [7–13]. Due to its high thermal and chemical stability in an oxidizing atmosphere [14–17], natural abundancy and non-toxicity, $CaMnO_{3-\delta}$ represent enormous promise for large scale thermoelectric applications for recovering waste heat from various industry sources such as cement manufacturing, steel making [18] or the combined heat and power applications in fuel cells [19–22].

Nevertheless, the compelling need for TE device is currently hindered by the low energy conversion efficiency of oxide thermoelectric materials. The thermoelectric materials for practical applications need to possess high conversion efficiency that is characterized by the dimensionless figure-of-merit [23], *ZT*. *ZT* is defined as $S^2\sigma T/\kappa$, where S is the Seebeck coefficient, σ is the electrical conductivity, $S^2\sigma$ is the electrical power factor, κ is the thermal conductivity, and *T* is the absolute temperature. The efficiency reaches about 10% when *ZT* = 1, and hence *ZT* $\geq$ 1 is generally accepted as a criterion for practical applications. In order to realize an efficient TE energy conversion, the following three physical properties are simultaneously required for TE materials. (1). Low thermal conductivity κ, which is necessary to introduce a large temperature difference between two ends of the materials (2). High electrical conductivity σ, which is required to reduce the internal resistance of the materials for carrier flow and (3). Large electromotive force (Seebeck Coefficient S), which is the driving force for the current flow to obtain a high voltage. $CaMnO_{3-\delta}$ possesses a substantial Seebeck coefficient around ∼ -600 μV/K at room temperature regime. For the single-crystalline [24] $CaMnO_{3-\delta}$, the theoretical calculation predicts the

ZT as high as 1.15 at 1000 K. The thermal conductivity of polycrystalline $CaMnO_{3-\delta}$ is very low, around 3.5 W/mK at room temperature regime. However, the electrical resistivity of polycrystalline $CaMnO_{3-\delta}$ is very high. A substantial amount of effort has been made to improve the thermoelectric properties of $CaMnO_{3-\delta}$ using the doping modification on either the Ca or Mn site, or both [25–33]. However, as for other TE materials, the Seebeck coefficient and the electrical conductivity are both functions of carrier concentration, the electrical conductivity increases as the carrier concentration and carrier mobility increase. At the same time, the Seebeck coefficient decreases as the carrier concentration increases. As a consequence, conventional doping for increasing the carrier concentration generally results in the simultaneous increase of electrical conductivity and a decrease of the Seebeck coefficient and eventually leads to a minimal increase in the overall power factor [34–37]. Some special fabricating methods, such as spark plasma sintering and spray drying, have been applied to further improve the thermoelectric performance [35]. Among the single-phase $CaMnO_{3-\delta}$ ceramics synthesized using different methods including spark plasma sintering [35], solid-state reaction [38], gas-phase reaction synthesis [39], chemical coprecipitation method [40], glycine–nitrate synthesis [41], electrostatic spray deposition [42], and soft chemistry synthesis (sol-gel) [43], the highest reported *ZT* of pristine [44] $CaMnO_{3-\delta}$ is 0.11, while the doped [45] $CaMnO_{3-\delta}$ possess the peaking *ZT* of 0.32.

Accordingly, despite the very high Seebeck coefficient and low thermal conductivity, the figure of merit *ZT* for ceramics $CaMnO_{3-\delta}$ remained to be very low. As such, there is a strong need to improve the thermoelectric performance of $CaMnO_{3-\delta}$ ceramics, especially to increase electrical conductivity. The polycrystalline ceramics materials have their physical properties strictly depending on the hierarchical structure. The hierarchical structure that has a dramatic impact on the transport properties of perovskite ceramics rang from the cation valence state, oxygen stoichiometry to the porosity, and the grain boundary nanostructures of the sintered ceramics. As such, the present work focus on investigating the impact of sintering temperature changes on the hierarchical structure and thermoelectric performance of pristine $CaMnO_{3-\delta}$. Upon the tuning of sintering temperatures for sintering of the $CaMnO_{3-\delta}$ ceramics with the powders precursor synthesized using the chemical sol-gel route, a *ZT* of 0.28 is obtained for the pristine $CaMnO_{3-\delta}$. This *ZT* of 0.28 is a factor of 2.5 higher than the highest reported *ZT* for pristine $CaMnO_{3-\delta}$ and approaches the one obtained for the doped $CaMnO_{3-\delta}$. Such high-performance pristine $CaMnO_{3-\delta}$ will be ideal for further performance enhancement using the doping. The atomic and nanoscale structure origin of the performance enhancement was systematically investigated.

2. Experimental procedure

The precursor powders for $CaMnO_{3-\delta}$ pellets were prepared by sol-gel reaction of $Ca(NO_3)_2$–$4H_2O$ (Calcium nitrate) and $Mn(NO_3)_2$–$4H_2O$ (Manganese nitrate) in stoichiometric ratios, mixed with citric acid and polyethylene glycol, and dissolved in a mix of deionized water, ethylene glycol and nitric acid. The mix was put on a hot stage, heated and stirred, in order to remove the water from the solution and to form the gel. The gel was ashed at 773 K in a Lindberg/Blue Thermo Scientific box furnace. The resulted ash was put in a planetary ball milling machine (Retsch PM 100) to obtain a fine powder. Then, the powder was calcined at 1173 K for 2 h in a tube furnace with oxygen flow. The calcined powder was mixed with 5 Polyvinyl butyral (PVB) and ethyl alcohol, heated on a hot stage, and stirred until dried. The resulted powder was manually ground again to obtain a fine powder. This powder was uniaxially pressed into pellets at 0.75 GPa at 423 K. The pellets were sintered at four different temperatures, 1273 K, 1373 K, 1473 K, and 1573 K, for 2 h, in a tube furnace with oxygen flow. The Seebeck coefficient and the electrical resistivity of the material were measured using Linseis LSR-1100 in a low pressure He environment, at a temperature range from 298 to 1073 K. The thermal conductivity of the samples was measured by a Laser Flash Analyzer (LFA) Linseis-1200 within a temperature range from 298 to

1073 K. The phase identification and crystal structure were characterized by X-ray diffraction using a Panalytical X'PertPro XRD with Cu Kα radiation at room temperature. The lattice parameters were determined by Rietveld refinement using the FullProf [46] software. The morphology and microstructure of the sintered samples were examined by scanning electron microscopy (SEM; Hitachi S-4700). TEM samples were prepared by mechanical polishing and ion milling in a liquid-nitrogen-cooled holder. Electron diffraction, diffraction contrast, and HRTEM imaging were performed using a JEM-2100 operated at 200 kV.

3. Results

3.1. Electrical properties

Fig. 1a displays the electrical resistivity (ρ) μΩm of the sintered samples of $CaMnO_{3-\delta}$ at different temperatures. For the samples sintered at 1273 K and 1373 K, the electrical resistivity at 380 K is very high, with values of 59240 μΩm and 53998 μΩm, respectively. On the other hand, sintering at 1473 K and 1573 K resulted in the decrease of magnitude of the electrical resistivity to 5329.29 μΩm and 6859.48 μΩm at 380 K. There is a continuous decrease in the electrical resistivity with the increase of measurement temperature for all samples. The lowest ρ were 321.28 μΩm, 188.44 μΩm, 262.35 μΩm, 209.95 μΩm at 1078 K for the samples sintered at 1273 K, 1373 K, 1473 K, and 1573 K. Seebeck coefficient (Fig. 1b) of all samples depict a negative value, indicating that the predominant charge carriers are electrons. For the samples sintered at different temperatures, the absolute value of the Seebeck Coefficient exhibits a different trend towards the increase of the measuring temperature. For the samples sintered at 1273 K and 1373 K, the Seebeck coefficient continued to increase with the increasing measuring temperature and peaked at 650–700 K. Further increase of the measurement temperature resulted in a decrease of the Seebeck coefficient. The maximum Seebeck coefficient value of the sample sintered at 1373 K was -593.42 μVK^{-1} at 564 K. The maximum Seebeck coefficient value of the sample sintered at 1273 K was -554.47 μVK^{-1} at 660 K. By contrast, for the samples sintered at 1473 K and 1573 K, there is a continuous decrease of the absolute value of the Seebeck coefficient while increasing the measuring temperature from 380 K to 1100 K. The highest value was -655.87 μVK^{-1} at 380 K for the sample sintered at 1573 K.

The power factor was calculated using $P = S^2/\rho$ (Fig. 1c). Due to the dramatically decreased electrical resistivity with the increase of the measurement temperature, the power factor of all samples increased with temperature. The increase in the sintering temperature has apparently increased the electrical power factor measured at different temperatures. The sample sintered at 1573 K exhibits the highest power factor that peaks at 1078 K with a value of 0.375 $mWm^{-1}K^{-2}$, and the maximum power factor of the sample sintered at 1373 K was 0.288 $mWm^{-1}K^{-2}$ at 1078 K.

3.2. Thermal conductivity and ZT

Thermal conductivity is calculated using the equation $\kappa = C_p \lambda \rho$, where C_p is the specific heat, λ is the thermal diffusivity, and ρ is the density. Thermal conductivity as a function of temperature is shown in Fig. 2a. The electronic thermal conductivity κ_{el} and the phonon (lattice) thermal conductivity κ_{ph} contribute to the total thermal conductivity of the materials, $\kappa = \kappa_{el} + \kappa_{ph}$, thus each component of the thermal conductivity can be analyzed independently. By considering the Wiedemann-Franz law $\kappa_{el} = L_0 T/\rho$, where L_0 is the Lorenz number (2.44×10^{-8} $W\Omega K^{-2}$), and ρ is the electrical resistivity, the electronic thermal conductivity (Fig. 2b) can be calculated, and thus the phonon thermal conductivity (Fig. 2c). The phonon thermal conductivity appears to be dominant for all samples. The value of *ZT* increases with temperature for all samples, as shown in Fig. 3. The highest *ZT* was 0.282 at 1073 K for the sample sintered at 1373 K. The peaking *ZT* at 1073 K of the samples sintered at 1273 K, 1473 K, and 1573 K are 0.245, 0.185, 0.204, respectively.
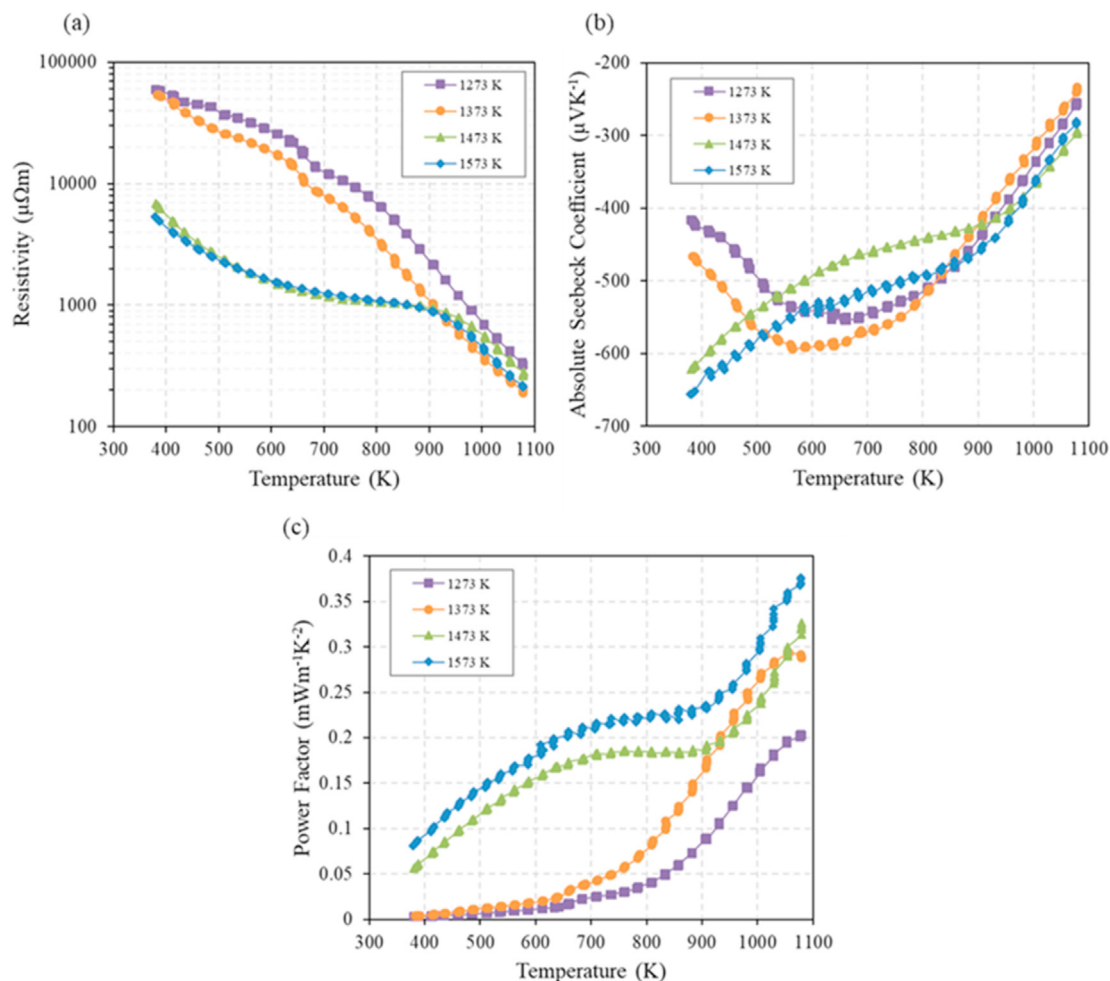
Fig. 1. Temperature dependence of electrical transport properties of $CaMnO_{3-\delta}$ (a). Electrical resistivity (b). Absolute Seebeck coefficient (c). Power Factor.

3.3. XRD lattice parameters and Mn–O distance

The X-ray diffraction patterns taken at room temperatures for $CaMnO_{3-\delta}$ sintered at different temperatures are shown in Fig. 4a. All diffraction peaks for the samples can be indexed as those $CaMnO_{3-\delta}$ [47], with an orthorhombic structure belonging to the *Pnma* (62) space group. All samples appear to be single-phase without the presence of the impurities. The lattice parameters obtained through Rietveld refinement are given in Table 1.

The lattice parameters systematically increase with increasing sintering temperature. The evolution of the lattice parameters and cell volume for samples sintered at different temperatures are shown in Fig. 4b. For the $CaMnO_{3-\delta}$ with the orthorhombic crystal structure, the unit cell orthorhombicity (Or) has been defined by the equation $Or(\%) = [(a-c)/(a+c)] \times 100$ with respect to the *c*-axis. This orthorhombicity can be used as a measure of the orthorhombic distortion [48]. Table 2 displays that there is a decrease in orthorhombicity with increasing the sintering temperature. As a result of Rietveld refinement, interatomic distances and angles are also obtained. Mn–O distances and angles were studied in order to analyze the influence of sintering temperature on octahedral tilting magnitude. A distorted orthorhombic structure is given in Fig. 4c. Table 2 comprises characteristics of distances and angles between Mn, Oa, and Op atoms. Average values of interatomic distances Mn–O present a small but continuous increase with an increase of sintering temperatures from 1273 K to 1373 K. Nevertheless, further increase of sintering temperature to 1473 K and 1573 K has largely changed the bond-lengths and bond angles.

3.4. Theoretical and apparent density of the pellets

Based on Rietveld refinement, the theoretical density was calculated using equation (1).

$$\rho = \frac{N_c A}{V_c N_A} \tag{1}$$

where N_c is the number of atoms in the unit cell, A is the atomic weight, V_c is the volume of the unit cell, and N_A is the Avogadro's number (6.022 $\times 10^{23}$ mol^{-1}). The calculated density for the pellets sintered at different temperatures is shown in Table 3. Those are comparable with the theoretical density of 4.59 g/cm^3 reported by Kennedy et al. [49]. Table 3 summarizes the density information of the $CaMnO_{3-\delta}$ sintered pellets, where apparent density is the density measured by the Archimedes method; the relative density is the ratio between apparent density and the theoretical density.

3.5. Grain morphology and grain sizes

The SEM images (Fig. 5) from all samples display the equiaxed grains. While the samples sintered at 1273 K and 1373 K present the uniform structure with a small grain size of ~895 nm and 1833 nm on average, respectively, the sample sintered at 1473 K depicts the bimodal distribution of the grain size with the bigger grain size of 5 μm and the small grain size of 1 μm. There is a significant increase in the grain size when the sintering temperature is increased to 1473 K and 1573 K. As plotted
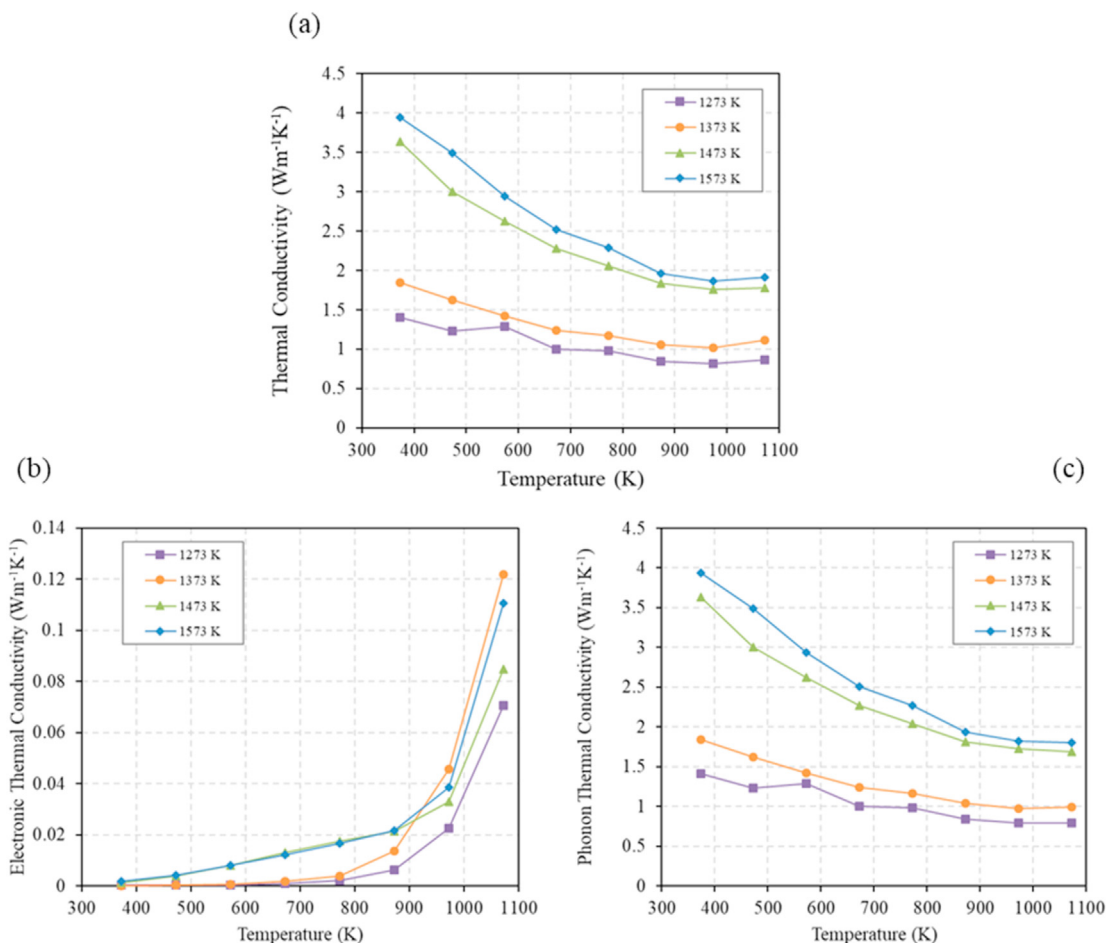
Fig. 2. Temperature dependence of the thermal conductivity of CaMnO$_{3-\delta}$. (a) Total thermal conductivity. (b) Electronic thermal conductivity. (c) Phonon thermal conductivity.

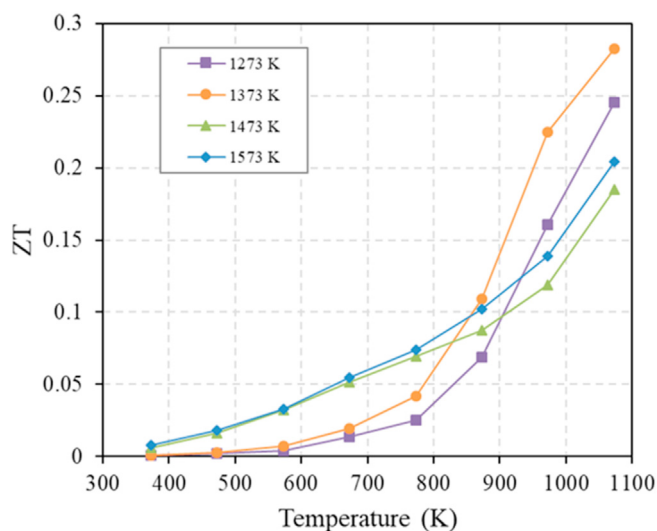**Fig. 3.** Temperature dependence of figure of merit ZT of CaMnO$_{3-\delta}$.

in Fig. 5e, both the lattice parameters and the density of the pellets increase with the sintering temperature.

3.6. Crystal defects

TEM nanostructure examination was performed on the samples sin-

tered at 1273 K, 1373 K, and 1573 K. Consistent with XRD analysis, there is no intergranular or intragranular secondary formation even at the nanoscale, as shown in Fig. 6. Samples sintered at 1273 K and 1373 K presents none or very few twinning. By contrast, there is a large amount of twinning for the samples sintered at 1473 K and, especially at 1573 K. The increased amount of twinning can be directly related to the increase of the lattice parameter difference between a/c or the increased ortho-rhombicity (Or) that is defined by the equation $Or(\%) = [(a-c)/(a+c)] \times 100$ with respect to the c-axis. The twinning is typical for perovskite materials. Including La$_{0.6}$Sr$_{0.4}$MnO$_3$ [50] and YBa$_2$Cu$_3$O$_7$ [51], for which the twinning is formed to accommodate the lattice parameter differences between a and c directions. The presence of the large-scale twinning can be directly correlated to the decrease in orthorhombicity while increasing the sintering temperature. Those nano twinning are having the width ranging from a single atomic layer to several nanometers, as shown in Fig. 6, that could affect the electrical and thermal conductivity.

4. Discussion

4.1. The large value of ZT from pristine CaMnO$_{3-\delta}$ ceramics and the hierarchical structure changes induced by controlling the sintering temperature

Table 4 shows a comparison between the figure of merit and power factor from this work with other reported values for different doped CaMnO$_{3-\delta}$ samples. It can be appreciated that the performance for this pristine CaMnO$_{3-\delta}$ is very close or even higher than other published
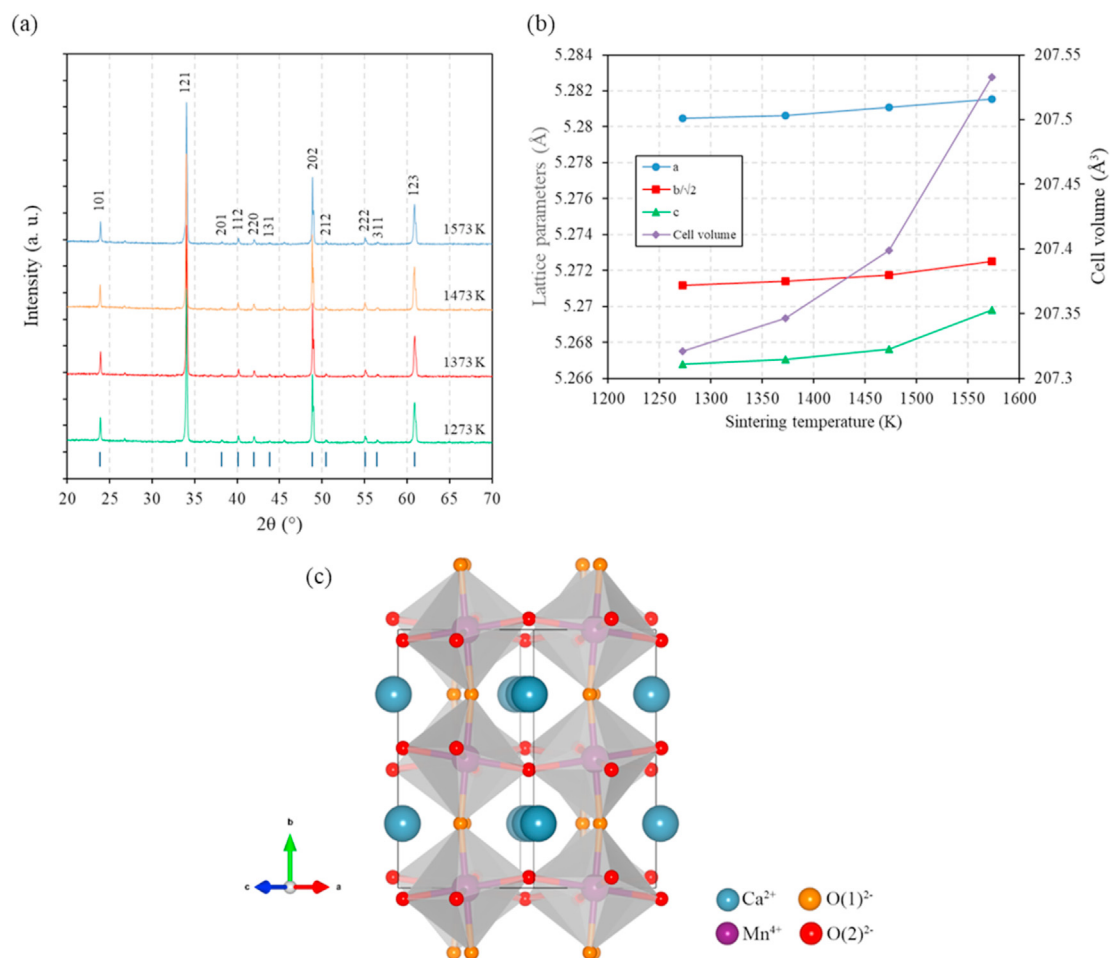
Fig. 4. (a) XRD patterns for CaMnO$_{3-\delta}$ sintered at 1273 K, 1373 K, 1473 K and 1573 K for 2 h. (b) Lattice parameters and cell volumes of CaMnO$_{3-\delta}$ as a function of sintering temperature. (c) Crystal structure of CaMnO$_{3-\delta}$. Positions of the O1 and O2 atoms.

**Table 1**
Refined lattice parameters of CaMnO$_{3-\delta}$.

	Sintered at 1273 K	Sintered at 1373 K	Sintered at 1473 K	Sintered at 1573 K
a (Å)	5.2805 (1)	5.2806 (1)	5.2811 (1)	5.2815 (1)
b (Å)	7.4546 (2)	7.4549 (2)	7.4553 (2)	7.4565 (2)
c (Å)	5.2668 (1)	5.2670 (1)	5.2675 (1)	5.2698 (1)
Volume (Å^3)	207.32 (1)	207.35 (1)	207.39 (1)	207.53 (1)
Ca				
x	0.0270	0.0258	0.0269	0.0241
y	0.2500	0.2500	0.2500	0.2500
z	−0.0091	−0.0108	−0.0082	−0.0089
Mn				
x	0.0000	0.0000	0.0000	0.0000
y	0.0000	0.0000	0.0000	0.0000
z	0.5000	0.5000	0.5000	0.5000
O$_1$				
x	0.4935	0.4945	0.4940	0.4948
y	0.2500	0.2500	0.2500	0.2500
z	0.0495	0.0491	0.0496	0.0490
O$_2$				
x	0.2927	0.2952	0.2992	0.2991
y	0.0387	0.0400	0.0359	0.0359
z	0.7005	0.7036	0.7005	0.7009
R_{wp}	17.7	17.9	18.2	21.6
R_{exp}	12.00	12.37	12.24	12.70
χ^2	2.17	2.09	2.20	2.90

Table 2
Interatomic distances and bond angles for CaMnO$_{3-\delta}$ sintered at different temperatures.

	1273 K	1373 K	1473 K	1573 K
Mn–O1a (2x) (Å)	1.8821 (3)	1.8818 (3)	1.8823 (3)	1.8821 (3)
Mn–O1p (2x) (Å)	1.9416 (2)	1.9225 (2)	1.9196 (1)	1.9186 (2)
Mn–O2p (2x) (Å)	1.8941 (2)	1.9153 (1)	1.9194 (1)	1.9205 (2)
<Mn-Op> (Å)	1.9179	1.9189	1.9195	1.9196
<Mn–O> (Å)	1.9059	1.9065	1.9071	1.9071
Mn-Oa-Mn (°)	163.93 (2)	164.11 (2)	163.91 (2)	164.15 (2)
Mn-Op-Mn (°)	152.90 (2)	152.66 (2)	152.56 (2)	152.67 (2)
<Mn–O–Mn> (°)	158.42	158.39	158.26	158.41
Or (%)	0.129749	0.128805	0.127475	0.111057

Table 3
Apparent densities of CaMnO$_{3-\delta}$.

| Sample	Apparent density (g/cm^3)	Calculated density (g/cm^3)	Relative density (%)
Sintered at 1273 K	3.0359	4.5820	66
Sintered at 1373 K	3.6209	4.5814	79
Sintered at 1473 K	4.2114	4.5803	92
Sintered at 1573 K	4.4254	4.5773	97
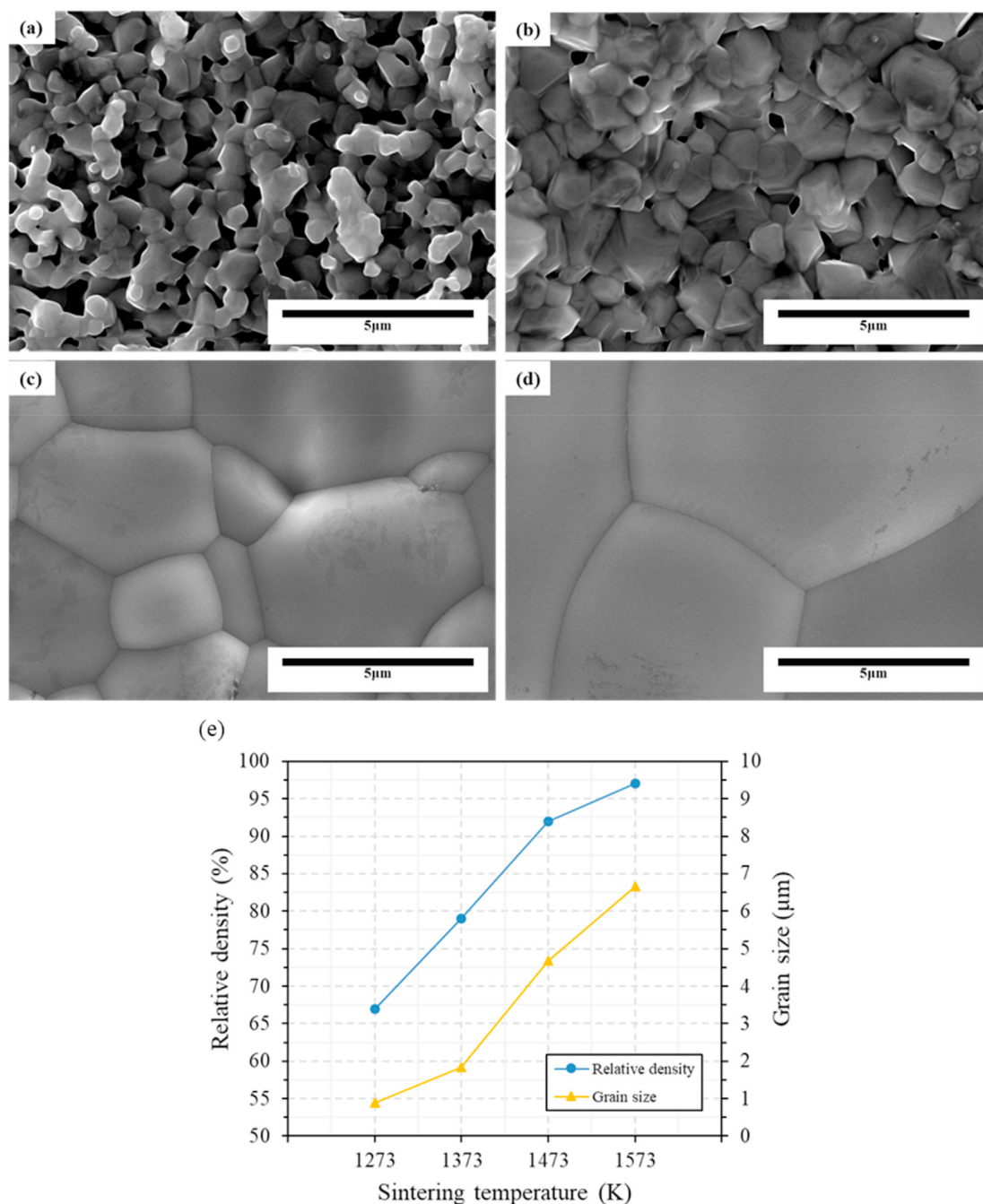
Fig. 5. SEM micrographs $CaMnO_{3-\delta}$ sintered at a) 1273 K, b) 1373 K, c) 1473 K, and d) 1573 K. e) Relative densities and grain size as a function of sintering temperature.

results from samples with different dopants. For the single-phase $CaMnO_{3-\delta}$, this is the highest electrical power factor and highest *ZT*.

Besides the large increase in the thermoelectric performance, there are also systematic changes in the structure from nano to micron scales. The simultaneous increase of the grain size and crystal density with the increase of the sintering temperature is intergraded into the 3D schematic shown in Fig. 7. The present results show that, except for the lattice parameter changes, the variation in the structure of oxide ceramics induced by simply controlling the sintering temperature is hierarchical. The different crystal structure changes from the unit cell level to the microns will simultaneously impact the Seebeck coefficient, electrical conductivity, and thermal conductivity.

4.2. Large variation of the seebeck coefficient

One of the biggest changes due to the sintering temperature is the Seebeck coefficient. For the samples sintered at 1273 K and 1373 K, the Seebeck coefficient is -415.95 µV/K, and -466.51 µV/K measured at 380 K. By contrast, the samples sintered at 1473 K and 1573 K, the Seebeck coefficient are -621.94 µV/K and -655.87 µV/K measured at 380 K. For oxide ceramics, the Seebeck coefficient is irrelevant to the grain boundary [55] and porosity for the pristine single phase without dopants segregation at the grain boundaries. Indeed, the Seebeck coefficient is intrinsic to the carrier concentration and the lattice distortion. The cell parameters obtained by Rietveld refinement of the XRD spectra
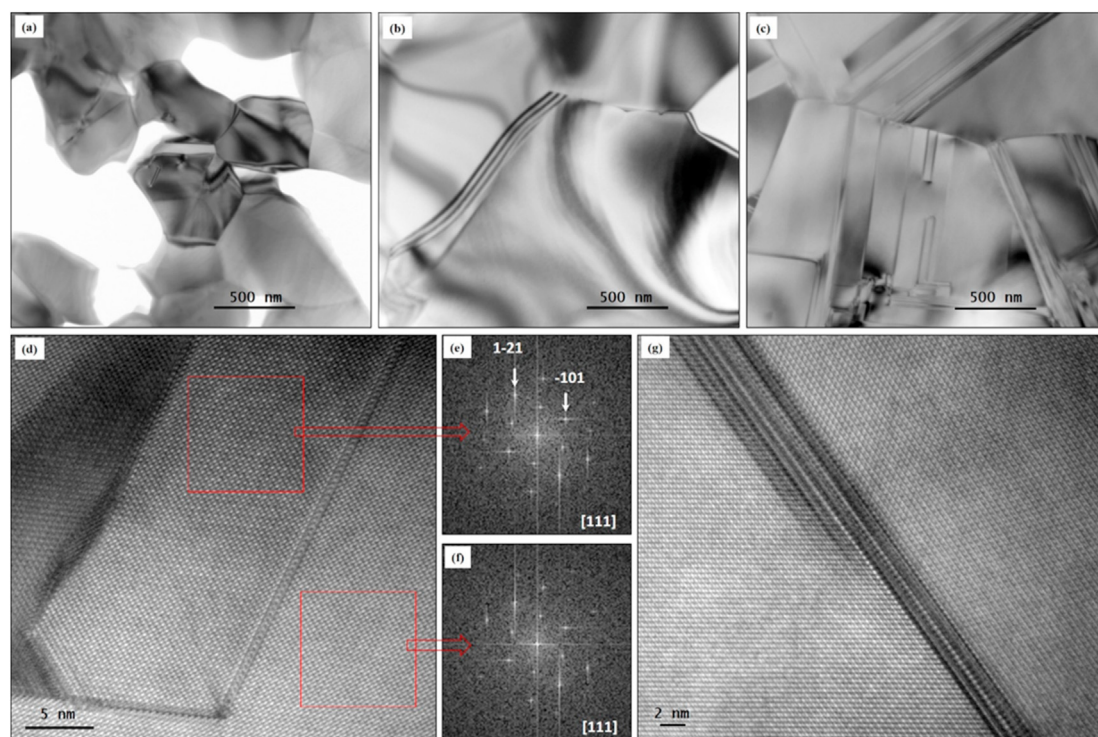
Fig. 6. TEM images of samples sintered at 1273 K (a), 1373 K (b), and 1573 K(c). (d) nano-twinning and related Fourier transformation (e) and (f). (g) There is also a twinning boundary with a thickness of ∼ 5 nm.

Table 4
The figure of merit and power factor of $CaMnO_3$ with different dopants.

Dopant	Temperature (K)	Power factor (mWm^{-1}K^{-2})	ZT
Nb [52]	1073	0.19	0.325
Dy, Ho, Er, Yb [53]	1000	0.2–0.35	0.15–0.2
W [31]	1073	0.32	0.16
Y, Dy codopants [38]	800	0.31	0.18
Pr, Yb codopants [54]	973	0.33	0.24
Pristine sample sintered at 1373 K (this study)	1073	0.29	0.28

for each sintering temperature are shown in Fig. 4. The lattice parameters are observed to increases with increasing sintering temperature. Since Ca^{2+} has a fixed valence and radii of 1.34 Å, the lattice parameters increase could be attributed to the ionic radius change or the increased ratio of Mn^{3+}/Mn^{4+}, which the radius of ions are Mn^{4+} (0.53 Å) and Mn^{3+} (0.645 Å) [56]. The lower sintering temperature resulted in the formation of a more oxidized manganese ion because this is stable preferentially as Mn^{4+} at lower temperatures. When the sintering temperature increases, the amount of Mn^{4+} decreases by liberating oxygen, which leads to a decrease in the Mn oxidation state. Such changes in the Mn valence state could also be related to the two distinct trends in the variation of the Seebeck Coefficient with temperature. As depicted in Fig. 1b, for the samples sintered at 1273 K, and 1373 K that is presumably with Mn^{4+}, at temperature region of 380 K–680 K, the absolute Seebeck coefficient decrease with the increasing temperature. By contrast, the samples sintered at 1473 K, and 1573 K, which are with an increased amount of Mn^{3+}, the absolute Seebeck Coefficient decrease with the increase of temperature. The present experimental results are fully consistent with the First Principle Calculation revealing the impact of reduced oxygen content on the Mn valence state, the electrical, structural, and thermoelectric properties [57]. The results from the current work further confirm that the presence of the mixed-valence state is likely to influence the gradient of the density of the states at the bottom of

the conduction band, the number of carriers, and the Seebeck coefficients [58].

The ionic valence state changes are also accompanied by the lattice distortion. There is a decrease in orthorhombicity with increasing the sintering temperature. This decrease in orthorhombicity is also accompanied by changes in bond angles. Changes in angle values represent structural changes as a result of octahedral tilting. In an ideal cubic structure, Mn–O1a-Mn and Mn–O1p-Mn angles are 180°. Mn–O1a-Mn represents tilting around axis *b*. Mn–O1p-Mn angle represents octahedral tilting around axes *a* and *c* [59]. There is a sharp change in both the bonding angle and orthorhombicity, as shown in Table 2. It is worthwhile to point out that such large changes in the Seebeck coefficient and changes in the unit cell distortion is also consistently reflected in the large crystal grain growth, as summarized in Fig. 7, that further affects the electrical conductivity of the samples.

4.3. Electrical and thermal conductivity origin of the increased ZT

Apparently, sintering at higher temperatures of 1473 K and 1573 K has largely increased the carrier concentration, especially at room temperature regimes, in comparison with that from the samples sintered at 1273 K and 1373 K. The electrical conductivity [25,28] of $CaMnO_{3-\delta}$ is governed by polaron hopping in the Mn^{4+} matrix. By increasing the Mn^{3+} concentration, there is increased carrier concentration for decreasing the Seebeck coefficient and increasing the intragranular electrical conductivity. Meanwhile, there is a sharp increase in the grain size or a decrease in the grain boundary density. Transport properties in the manganite perovskite system are very sensitive to Mn–O bond length and Mn–O–Mn bond angle [60]. Like those from samples sintered at 1273 K and 1373 K, Smaller grains have more broken Mn–O–Mn bonds at the grain boundaries that block the electron conduction and increase the resistivity. When the grain boundary density decreases, the scattering of electrons is reduced by the grain boundaries. This reduction of the grain boundary density improves the connections between the grains in the material, leading to a decrease in the carrier scattering at the grain
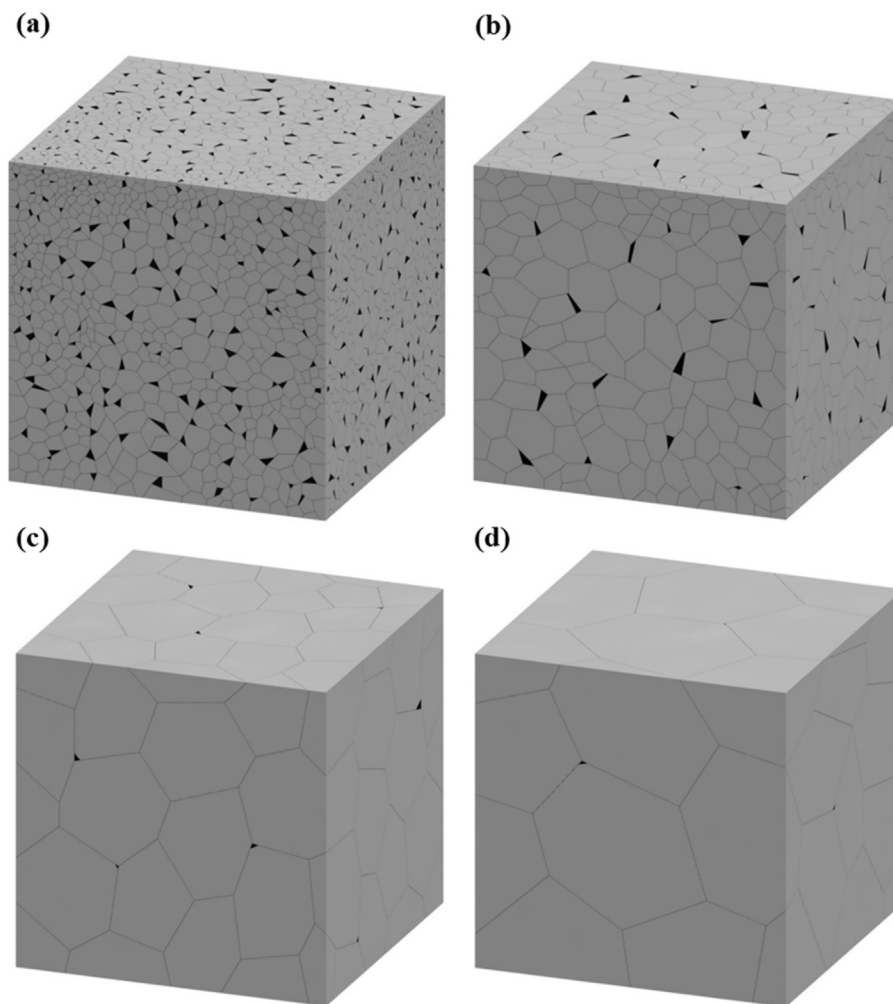
Fig. 7. Evolution of the grain morphology in CaMnO$_{3-\delta}$ sintered at (a) 1273 K, (b) 1373 K, (c) 1473 K, and (d) 1573 K.

boundaries, increasing the carrier mobility. In other words, the reduction of electrical resistivity could be, in part, attributed to the decreasing grain boundary density when sintering temperature increases.

4.4. Impact of the nanostructure on the thermal properties

The increase of electrical conductivity has primarily increased the power factor and the *ZT* at lower temperature regimes. However, in comparison with the samples sintered at 1573 K that present the highest power factor, the peaking *ZT* of 0.28 achieved in the sample sintered at 1373 K is attributed to the large decrease of the thermal conductivity. In general, the thermal conductivity is insensitive to carrier concentration as the largest contribution is from the lattice vibrations. Therefore, the conductivity is normally sensitive to both distortions in the lattice and weight differences of atoms. To lower the conductivity, the dopant should be larger than the doped element and heavier, where the mass difference is the dominating factor. In the present study, since all samples are pristine single phase, the large change in the thermal conductivity is mostly affected by the nanostructure, including both the grain boundaries and the porosity.

4.4.1. Impact of grain boundaries on the thermal conductivity

The thermal boundary resistance between two grains of the same material is sometimes referred to as the Kapitza resistance [61], although this term is also used to describe the thermal resistance between solid/solid interfaces of different materials or solid/liquid interfaces. The

Kapitza resistance can commonly exist in polycrystals, and its overall effect is to reduce the thermal conductivity of polycrystals. This resistance could be calculated theoretically using the approximation adopted by Nan and Birringer [62]:

$$\frac{1}{\kappa} = \frac{1}{\kappa_o} + \frac{2R_K}{D} \tag{2}$$

where κ is the thermal conductivity, κ_o the bulk thermal conductivity (the Maxwell-Eucken equation was used to predict the bulk thermal conductivity κ_o [62]). Since the measured thermal conductivity shown in Fig. 2 presents the convolution of both the grain boundary and porosity in the actual samples, in order to make equation (2) feasible, the κ values need to be taken from the fully dense sample without porosity. Since the sample sintered at 1573 K has a 97% density, as shown in Table 3, the measured thermal conductivity of 3.943 W/mK was assumed as that from the 100% dense sample. Taking the actual grain size and the κ_o, R_K, the Kapitza resistance for the sample sintered at 1573 K was calculated using equation (2) and listed in Table 5. Taking R_K from the sample sintered at 1573 K and factoring the Kapitza resistance to the remaining samples using the grain size difference, the R_K of the samples are deduced and shown in Table 5.

As we mentioned before, the overall effect of the Kapitza resistance is to reduce the thermal conductivity of polycrystals. Also, from equation (2) it can be deduced that κ could be further decreased if even smaller grain sizes could be achieved. Based on the deduced R_K, the thermal conductivity κ was calculated using the equation for the samples sintered

Table 5
Kapitza resistance at 373 K calculated for CaMnO$_{3-\delta}$ sintered at different temperatures.

Sample	κ (W/mK)	κ_o (W/mK)	D (μm)	R_K (m^{2}K/W)
Sintered at 1273 K	2.465	2.616	0.895	1.0486×10^{-8}
Sintered at 1373 K	2.622	2.660	1.833	5.1200×10^{-9}
Sintered at 1473 K	4.150	4.165	4.683	2.0041×10^{-9}
Sintered at 1573 K	3.943	3.950	6.666	1.4079×10^{-9}

at 1273 K, 1373 K, and 1473 K, respectively, as shown in Table 5. Once again, the κ value in Table 5 is the estimated values for the 100% dense sample with different grain sizes. Those calculated κ values indicate that, for the 100% dense sample, when the grain size is reduced from 6.6 μm to 0.9 μm, the thermal conductivity is actually reduced from 3.9 W/mK to 2.5 W/mK, which represent the 36% reduction. Apparently, the Kapitza resistance and the thermal conductivity can be further decreased if the samples with smaller grains such as 100 nm could be further achieved.

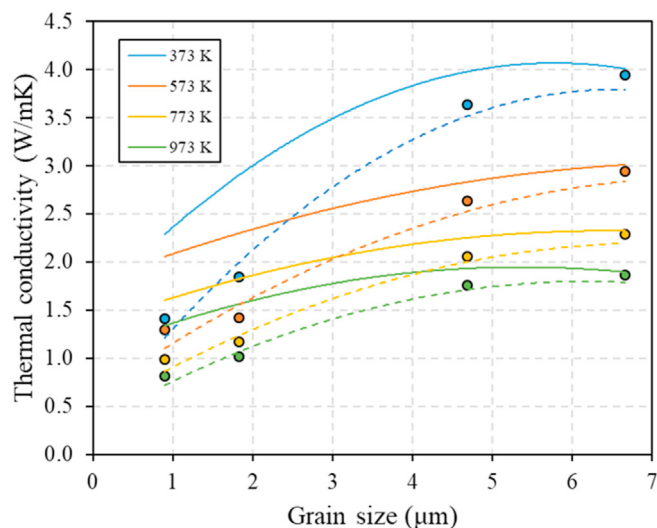### 4.4.2. Impact of porosity on the thermal conductivity

Table 3 shows that there is a significant change in the porosity of the samples sintered at different temperatures. To further investigate the effect of porosity on the phonon thermal conductivity, the Maxwell-Eucken equation was used to predict the bulk thermal conductivity κ_o [63], which was derived in a similar analysis by Mi et al. [64]. The effect of porosity on the total thermal conductivity can be estimated by solving the equation $\kappa = \kappa_o v/(1 + \beta(1 - v))$, where v is the volume fraction (relative density) of the material, κ is the measured total thermal conductivity with porosity, κ_o is the bulk thermal conductivity and β is the pore shape factor, which was selected as $\beta = 2/3$ indicating randomly dispersed cylindrical pores [65]. The bulk thermal conductivity κ_o of the assumed 100% density with the grain boundaries of all samples is taken for the estimated thermal conductivity in Table 5 and registered in Table 6. Based on the Maxwell-Eucken equation [63], the κ values for different samples were estimated, as shown in Table 6. These values were estimated at 373 K and are significantly lower than the theoretical thermal conductivity values, indicating that the porosity has resulted in the reduction of thermal conductivity.

As such, the thermal conductivity of the samples is lowered by 46%, 31%, 13%, and 5% due to the porosity for the samples sintered at 1273 K, 1373 K, 1473 K, and 1573 K, respectively. Fig. 8 displays the integration of the calculated thermal conductivity with the consideration of the grain boundary density and porosity. Fig. 8 shows the theoretical calculation of the polycrystalline sample with 100% density (solid line) and with the actual porosity (dash line). To verify the accuracy of the theoretical calculations, the measured thermal conductivity data point (from Fig. 2) for the samples with different grain sizes is also displayed as an overlay with the theoretical calculation. Tables 5 and 6, and Fig. 8 clearly elucidate that both the grain boundary and the porosity have significantly reduced the thermal conductivity. Furthermore, the twin boundary shown in Fig. 6 could also play a significant role in scattering phonons and lowering the thermal conductivity. In the present study, due to the

Table 6
Estimated and theoretical thermal conductivity of samples with different relative density.

Sample	β	v (%) Measured value	κ (W/mK) Estimated Value	κ_o (W/mK) Theoretical value	κ/κ_o (%)
Sintered at 1273 K	2/3	66	1.326	2.465	53.80
Sintered at 1373 K	2/3	79	1.817	2.622	69.30
Sintered at 1473 K	2/3	92	3.625	4.150	87.34
Sintered at 1573 K	2/3	97	3.750	3.943	95.10

Fig. 8. Grain size dependence of thermal conductivity with contribution from porosity for CaMnO$_{3-\delta}$ (373 K, 573 K, 773 K, and 973 K). Solid lines represent the thermal conductivity of polycrystalline samples with 100% density. The dashed line shows the calculated value of thermal conductivity of polycrystalline samples with actual density. Marks represents experimental data.

facts that twins are largely absent for the samples sintered at 1273 K and 1373 K, the impact of the twins on the thermal conductivity are not considered.

4.5. Significance of tuning and controlling the sintering conditions of oxide perovskite

Perovskite compounds are usually synthesized with a wide variety of combinations of chemical elements in the cation sites, and electroneutrality is further facilitated by the vacancy formation. As a result of various dopants, the Perovskite present insulating, semiconducting, ionic conducting and superconducting, and viable for applications in different technology such as sensing devices, catalysts, and fuel cells. As such, the perovskite oxide offers tunability in terms of dopants. However, it is also critical to tune the performance of the pristine materials by controlling the materials synthesis conditions. For perovskite CaMnO$_{3-\delta}$, it is well recognized that the oxygen stoichiometry [66] has a large impact on the crystal structure and the conductivity. The orthorhombic phase is stable at 700–950 °C when $\delta < 0.04$. The phase transition from the orthorhombic to tetragonal structure occurs in the narrow range of $0.02 < \delta < 0.04$. For the present study, all samples are sintered under the same oxygen flow. Accordingly, the large variations in the Seebeck coefficient and the magnitude change of the electrical conductivity and thermal conductivity signify the importance of carefully tuning the pristine ceramics that could be further employed as the baseline of further dopants. Based on the optimized baseline performance, incorporating dopants into the lattice and composite at the grain boundaries has enhanced the ZT to 0.67 [67]. Due to the significant impact of the grain boundaries and porosity on the thermal conductivity as revealed by the present study, further ZT improvement could be further made by tuning the dopants or the ceramics processing conditions.

5. Conclusion

The present work demonstrated that even for pristine perovskite CaMnO$_{3-\delta}$, the thermoelectric ZT had been increased to 0.28, which is a factor of 2.5 higher than the ZT of 0.11 of pristine CaMnO$_{3-\delta}$ synthesized using other methods. The sintering temperature has a significant impact on the hierarchical structure that was ranging from unit lattice distortion, nano twinning to the grain size and porosity. Those hierarchical structure

changes subsequently affect the electrical and thermal conductivities. The present work is instrumental in providing the processing principle for perovskite thermoelectric ceramics and in facilitating the design guidance of the perovskite family oxides that share many common physical properties.

CRediT authorship contribution statement

Sergio A. Paredes-Navia: Conceptualization, Methodology, Investigation, Formal analysis, Data curation, Writing - original draft, Writing - review & editing. **Liang Liang:** Methodology, Investigation. **Cesar-Octavio Romo-De-La-Cruz:** Methodology, Investigation, Writing - review & editing. **Ellena Gemmen:** Writing - review & editing. **Andre Fernandes:** Writing - review & editing. **Jacky Prucz:** Conceptualization, Writing - review & editing, Supervision. **Yun Chen:** Conceptualization, Methodology, Investigation, Writing - original draft, Writing - review & editing, Supervision. **Xueyan Song:** Conceptualization, Methodology, Investigation, Formal analysis, Data curation, Writing - original draft, Writing - review & editing, Supervision, Project administration, Funding acquisition.

Declaration of competing interest

The authors declare that they have no known competing financial interests or personal relationships that could have appeared to influence the work reported in this paper.

Acknowledgments

References

[1] J.B. MacChesney, H.J. Williams, R.C. Sherwood, J.F. Potter, Magnetic study of the manganate phases: $CaMnO_3$, $Ca_4Mn_3O_{10}$, $Ca_3Mn_2O_7$, Ca_2MnO_4, J. Appl. Phys. 39 (1968) 1206, https://doi.org/10.1063/1.1656225.

[2] M. Ohtaki, H. Koga, T. Tokunaga, K. Eguchi, H. Arai, Electrical transport properties and high-temperature thermoelectric performance of $(Ca_{0.9}M_{0.1})MnO_3$ (M = Y, La, Ce, Sm, in, Sn, Sb, Pb, Bi), J. Solid State Chem. 120 (1995) 105–111, https://doi.org/10.1006/jssc.1995.1384.

[3] J.M.D. Coey, M. Viret, S. von Molnár, Mixed-valence manganites, Adv. Phys. 48 (1999) 167–293, https://doi.org/10.1080/000187399243455.

[4] B. Raveau, Y.M. Zhao, C. Martin, M. Hervieu, A. Maignan, Mn-site doped $CaMnO_3$: creation of the CMR effect, J. Solid State Chem. 149 (2000) 203–207, https://doi.org/10.1006/jssc.1999.8517.

[5] P. Carvillo, Y. Chen, C. Boyle, P.N. Barnes, X. Song, Thermoelectric performance enhancement of calcium cobaltite through barium grain boundary segregation, Inorg. Chem. 54 (2015) 9027–9032, https://doi.org/10.1021/acs.inorgchem.5b01296.

[6] C. Romo-De-La-Cruz, L. Liang, S.A.P. Navia, Y. Chen, J. Prucz, X. Song, Role of oversized dopant potassium on the nanostructure and thermoelectric performance of calcium cobaltite ceramics, Sustain. Energy Fuels. 2 (2018) 876–881, https://doi.org/10.1039/C7SE00612H.

[7] T. Zhu, Y. Liu, C. Fu, J.P. Heremans, J.G. Snyder, X. Zhao, Compromise and synergy in high-efficiency thermoelectric materials, Adv. Mater. 29 (2017) 1605884, https://doi.org/10.1002/adma.201605884.

[8] K.R. Talley, S.C. Barron, N. Nguyen, W. Wong-Ng, J. Martin, Y.L. Zhang, X. Song, Thermoelectric properties of the $LaCoO_3$-$LaCrO_3$ system using a high-throughput combinatorial approach, Solid State Sci. 64 (2017) 7–12, https://doi.org/10.1016/j.solidstatesciences.2016.12.002.

[9] R.J. Mehta, Y. Zhang, C. Karthik, B. Singh, R.W. Siegel, T. Borca-Tasciuc, G. Ramanath, A new class of doped nanobulk high-figure-of-merit thermoelectrics by scalable bottom-up assembly, Nat. Mater. 11 (2012) 233–240, https://doi.org/10.1038/nmat3213.

[10] J. Yang, F.R. Stabler, Automotive applications of thermoelectric materials, J. Electron. Mater. 38 (2009) 1245–1251, https://doi.org/10.1007/s11664-009-0680-z.

[11] Y. Pei, X. Shi, A. LaLonde, H. Wang, L. Chen, G.J. Snyder, Convergence of electronic bands for high performance bulk thermoelectrics, Nature 473 (2011) 66–69, https://doi.org/10.1038/nature09996.

[12] M.S. Dresselhaus, G. Chen, M.Y. Tang, R.G. Yang, H. Lee, D.Z. Wang, Z.F. Ren, J.-P. Fleurial, P. Gogna, New directions for low-dimensional thermoelectric materials, Adv. Mater. 19 (2007) 1043–1053, https://doi.org/10.1002/adma.200600527.

[13] U.S. Department, Of Energy, Combined Heat and Power Technology Fact Sheet Series, Overview of CHP Technologies, 2016.

[14] J. He, T.M. Tritt, Advances in thermoelectric materials research: looking back and moving forward, Science 357 (80) (2017), eaak9997, https://doi.org/10.1126/science.aak9997.

[15] C. Wang, L. Shi, X. Xu, S. Zhou, J. Zhao, Y. Guo, H. Liu, L. He, X. Cai, G. Xu, High-temperature thermoelectric characteristics of B-site substituted $Yb_{0.1}Ca_{0.9}Mn_{1-x}Nb_xO_3$ system ($0 \leq x \leq 0.1$), Appl. Phys. A 112 (2013) 1003–1009, https://doi.org/10.1007/s00339-012-7465-6.

[16] A. Bhaskar, C.-J. Liu, J.J. Yuan, C.-L. Chang, Thermoelectric properties of n-type $Ca_{1-x}Bi_xMn_{1-y}Si_yO_{3-\delta}$ (x=y=0.00, 0.02, 0.03, 0.04, and 0.05) system, J. Alloys Compd. 552 (2013) 236–239, https://doi.org/10.1016/j.jallcom.2012.10.078.

[17] R. Kabir, T. Zhang, R. Donelson, D. Wang, R. Tian, T.T. Tan, B. Gong, S. Li, Thermoelectric properties of Yb and Nb codoped $CaMnO_3$, Phys. Status Solidi 211 (2014) 1200–1206, https://doi.org/10.1002/pssa.201330475.

[18] D. Champier, Thermoelectric generators: a review of applications, Energy Convers. Manag. 140 (2017) 167–181, https://doi.org/10.1016/j.enconman.2017.02.070.

[19] Y. Chen, K. Gerdes, S.A. Paredes Navia, L. Liang, A. Hinerman, X. Song, Conformal electrocatalytic surface nanoionics for accelerating high-temperature electrochemical reactions in solid oxide fuel cells, Nano Lett. 19 (2019) 8767–8773, https://doi.org/10.1021/acs.nanolett.9b03515.

[20] U.S. Department, Of Energy, Quadrennial Technology Review (Chapter 6):, in: Innovating Clean Energy Technologies in Advanced Manufacturing, Technology Assessments, Additive Manufacturing, 2015, 2015.

[21] B. Orr, A. Akbarzadeh, Prospects of waste heat recovery and power generation using thermoelectric generators, Energy Procedia 110 (2017) 250–255, https://doi.org/10.1016/j.egypro.2017.03.135.

[22] O. Francis, I. Kingsley, Assessment of economic impact and efficiency of a combined gas turbine with a thermoelectric generator, Int. J. Multidiscip. Sci. Eng. 3 (2012) 1–6.

[23] K.A. Borup, J. de Boor, H. Wang, F. Drymiotis, F. Gascoin, X. Shi, L. Chen, M.I. Fedorov, E. Müller, B.B. Iversen, G.J. Snyder, Measuring thermoelectric transport properties of materials, Energy Environ. Sci. 8 (2015) 423–435, https://doi.org/10.1039/C4EE01320D.

[24] F.P. Zhang, Q.M. Lu, X. Zhang, J.X. Zhang, Electrical transport properties of $CaMnO_3$ thermoelectric compound: a theoretical study, J. Phys. Chem. Solid. 74 (2013) 1859–1864, https://doi.org/10.1016/j.jpcs.2013.07.019.

[25] Y. Wang, Y. Sui, H. Fan, X. Wang, Y. Su, W. Su, X. Liu, High temperature thermoelectric response of electron-doped $CaMnO_3$, Chem. Mater. 21 (2009) 4653–4660, https://doi.org/10.1021/cm901766y.

[26] P.X. Thao, T. Tsuji, M. Hashida, Y. Yamamura, High temperature thermoelectric properties of $Ca_{1-x}Dy_xMnO_{2.98}$ ($0 <= x <= 0.2$), J. Ceram. Soc. Japan. 111 (2003) 544–547, https://doi.org/10.2109/jcersj.111.544.

[27] D. Flahaut, T. Mihara, R. Funahashi, N. Nabeshima, K. Lee, H. Ohta, K. Koumoto, Thermoelectrical properties of A-site substituted $Ca_{1-x}Re_xMnO_3$ system, J. Appl. Phys. 100 (2006) 84911, https://doi.org/10.1063/1.2362922.

[28] Y. Wang, Y. Sui, X. Wang, W. Su, Effects of substituting La^{3+}, Y^{3+} and Ce^{4+} for Ca^{2+} on the high temperature transport and thermoelectric properties of $CaMnO_3$, J. Phys. D Appl. Phys. 42 (2009) 55010, https://doi.org/10.1088/0022-3727/42/5/055010.

[29] A. Bhaskar, J.J. Yuan, C.-J. Liu, Thermoelectric properties of n-type $Ca_{1-x}Bi_xMnO_{3-\delta}$ (0.00, 0.02, and 0.05) system, J. Electroceram. 31 (2013) 124–128, https://doi.org/10.1007/s10832-013-9811-2.

[30] G. Xu, R. Funahashi, Q. Pu, B. Liu, R. Tao, G. Wang, Z. Ding, High-temperature transport properties of Nb and Ta substituted $CaMnO_3$ system, Solid State Ionics 171 (2004) 147–151, https://doi.org/10.1016/S0167-2738(03)00108-5.

[31] R. Kabir, T. Zhang, D. Wang, R. Donelson, R. Tian, T.T. Tan, S. Li, Improvement in the thermoelectric properties of $CaMnO_3$ perovskits by W doping, J. Mater. Sci. 49 (2014) 7522–7528, https://doi.org/10.1007/s10853-014-8459-x.

[32] A. Maignan, C. Martin, C. Autret, M. Hervieu, B. Raveau, J. Hejtmanek, Structural–magnetic phase diagram of Mo-substituted $CaMnO_3$: consequences for thermoelectric power properties, J. Mater. Chem. 12 (2002) 1806–1811, https://doi.org/10.1039/B200495J.

[33] Y. Zhou, I. Matsubara, R. Funahashi, G. Xu, M. Shikano, Influence of Mn-site doped with Ru on the high-temperature thermoelectric performance of $CaMnO_{3-\delta}$, Mater. Res. Bull. 38 (2003) 341–346, https://doi.org/10.1016/S0025-5408(02)00997-2.

[34] J.W. Park, D.H. Kwak, S.H. Yoon, S.C. Choi, Thermoelectric properties of Bi, Nb co-substituted $CaMnO_3$ at high temperature, J. Alloys Compd. 487 (2009) 550–555, https://doi.org/10.1016/j.jallcom.2009.08.012.

[35] H. Muguerra, B. Rivas-Murias, M. Traianidis, C. Marchal, P. Vanderbemden, B. Vertruyen, C. Henrist, R. Cloots, Thermoelectric properties of n-type $Ca_{1-x}Dy_xMn_{1-y}Nb_yO_{3-\delta}$ compounds (x=0, 0.02, 0.1 and y=0, 0.02) prepared by spray-drying method, J. Alloys Compd. 509 (2011) 7710–7716, https://doi.org/10.1016/j.jallcom.2011.04.056.

[36] A. Nag, R.S.C. Bose, High temperature transport properties of co-substituted $Ca_{1-x}Ln_xMn_{1-x}Nb_xO_3$ (Ln=Yb, Lu; $0.02 \leq x \leq 0.08$), Mater. Res. Bull. 74 (2016) 41–49, https://doi.org/10.1016/j.materresbull.2015.10.016.

[37] T. Reimann, J. Töpfer, Thermoelectric properties of Gd/W double substituted calcium manganite, J. Alloys Compd. 699 (2017) 788–795, https://doi.org/10.1016/j.jallcom.2016.12.359.

[38] J.W. Seo, J. Cha, S.O. Won, K. Park, Electrical transport and thermoelectric properties of $Ca_{0.8}Y_{0.2-x}Dy_xMnO_{3-\delta}$ ($0 \leq x \leq 0.2$), J. Am. Ceram. Soc. 100 (2017) 3608–3617, https://doi.org/10.1111/jace.14898.

[39] K. Koumoto, Y. Wang, R. Zhang, A. Kosuga, R. Funahashi, Oxide thermoelectric materials: a nanostructuring approach, Annu. Rev. Mater. Res. 40 (2010) 363–394, https://doi.org/10.1146/annurev-matsci-070909-104521.

[40] J. Lan, Y.-H. Lin, H. Fang, A. Mei, C.-W. Nan, Y. Liu, S. Xu, M. Peters, High-temperature thermoelectric behaviors of fine-grained Gd-doped $CaMnO_3$ ceramics,

J. Am. Ceram. Soc. 93 (2010) 2121–2124, https://doi.org/10.1111/j.1551-2916.2010.03673.x.

[41] I.A. Leonidov, E.I. Konstantinova, M. V Patrakeev, A.A. Markov, V.L. Kozhevnikov, Electrical conductivity and carrier mobility in $Ca_{1-x}Pr_xMnO_{3-\delta}$ manganites, Inorg. Mater. 53 (2017) 589–594, https://doi.org/10.1134/S0020168517060103.

[42] K. Fujimoto, M. Gibu, Y. Yamaguchi, A. Aimi, K. Nishio, O. Rabin, I. Takeuchi, Thermoelectric properties of bismuth-substituted calcium manganite $Ca_{1-x}Bi_xMnO_{3-\delta}$ prepared via the electrostatic spray deposition method, J. Ceram. Soc. Japan. 125 (2017) 308–312, https://doi.org/10.2109/jcersj2.16277.

[43] L. Bocher, M.H. Aguirre, R. Robert, D. Logvinovich, S. Bakardjieva, J. Hejtmanek, A. Weidenkaff, High-temperature stability, structure and thermoelectric properties of $CaMn_{1-x}Nb_xO_3$ phases, Acta Mater. 57 (2009) 5667–5680, https://doi.org/10.1016/j.actamat.2009.07.062.

[44] X.Y. Huang, Y. Miyazaki, T. Kajitani, High temperature thermoelectric properties of $Ca_{1-x}Bi_xMn_{1-y}V_yO_{3-\delta}$ ($0 \leq x = y \leq 0.08$), Solid State Commun. 145 (2008) 132–136, https://doi.org/10.1016/j.ssc.2007.10.012.

[45] L. Bocher, M.H. Aguirre, D. Logvinovich, A. Shkabko, R. Robert, M. Trottmann, A. Weidenkaff, $CaMn_{1-x}Nb_xO_3$ ($x \leq 0.08$) perovskite-type phases as promising new high-temperature n-type thermoelectric materials, Inorg. Chem. 47 (2008) 8077–8085, https://doi.org/10.1021/ic800463s.

[46] J. Rodriguez-Carvajal, FULLPROF: a program for Rietveld refinement and pattern matching analysis. Satell. Meet. Powder Diffr. XV, Congr. IUCr, 1990.

[47] Z.N. Jiang, F.P. Zhang, X. Zhang, Q.M. Lu, J.X. Zhang, Preparation and thermoelectric properties of the rare earths doped $Ca_{0.95}RE_{0.05}MnO_3$ (RE=Pr, Eu and Tb) oxide materials, Indian J. Pure Appl. Phys. 53 (2015) 530–536.

[48] P. Thiel, S. Populoh, S. Yoon, G. Saucke, K. Rubenis, A. Weidenkaff, Charge-carrier hopping in highly conductive $CaMn_{1-x}M_xO_{3-\delta}$ thermoelectrics, J. Phys. Chem. C 119 (2015) 21860–21867, https://doi.org/10.1021/acs.jpcc.5b05882.

[49] Q. Zhou, B.J. Kennedy, Thermal expansion and structure of orthorhombic $CaMnO_3$, J. Phys. Chem. Solid. 67 (2006) 1595–1598, https://doi.org/10.1016/j.jpcs.2006.02.011.

[50] Y. Chen, Y. Fan, S. Lee, G. Hackett, H. Abernathy, K. Gerdes, X. Song, Interface and grain boundary degradation in LSM-YSZ composite Solid Oxide Fuel Cell cathodes operated in humidified air, J. Power Sources 438 (2019) 227043, https://doi.org/10.1016/j.jpowsour.2019.227043.

[51] X. Song, J. Daniels, D.M. Feldmann, A. Gurevich, D. Larbalestier, Electromagnetic, atomic structure and chemistry changes induced by Ca-doping of low-angle $YBa_2Cu_3O_{7-\delta}$ grain boundaries, Nat. Mater. 4 (2005) 470–475, https://doi.org/10.1038/nmat1394.

[52] L. Bocher, M.H. Aguirre, D. Logvinovich, A. Shkabko, R. Robert, M. Trottmann, A. Weidenkaff, $CaMn_{1-x}Nb_xO_3$ ($x \leq 0.08$) perovskite-type phases as promising new high-temperature n-type thermoelectric materials, Inorg. Chem. 47 (2008) 8077–8085, https://doi.org/10.1021/ic800463s.

[53] Y. Wang, Y. Sui, W. Su, High temperature thermoelectric characteristics of $Ca_{0.9}R_{0.1}MnO_3$ (R=La,Pr,…,Yb), J. Appl. Phys. 104 (2008) 93703, https://doi.org/10.1063/1.3003065.

[54] C. Li, Q. Chen, Y. Yan, Effects of Pr and Yb dual doping on the thermoelectric properties of $CaMnO_3$, Mater. (Basel, Switzerland) 11 (2018) 1807, https://doi.org/10.3390/ma11101807.

[55] S. Chen, X. Song, X. Chen, Y. Chen, E.J. Barbero, E.L. Thomas, P.N. Barnes, Effect of precursor calcination temperature on the microstructure and thermoelectric properties of $Ca_3Co_4O_9$ ceramics, J. Sol. Gel Sci. Technol. 64 (2012) 627–636, https://doi.org/10.1007/s10971-012-2894-4.

[56] R.D. Shannon, Revised effective ionic radii and systematic studies of interatomic distances in halides and chalcogenides, Acta Crystallogr. A 32 (1976) 751–767, https://doi.org/10.1107/S0567739476001551.

[57] M. Molinari, D.A. Tompsett, S.C. Parker, F. Azough, R. Freer, Structural, electronic and thermoelectric behaviour of $CaMnO_3$ and $CaMnO_{(3-\delta)}$, J. Mater. Chem. A. 2 (2014) 14109–14117, https://doi.org/10.1039/C4TA01514B.

[58] E.-S. Lee, S. Cho, H.-K. Lyeo, Y.-H. Kim, Seebeck effect at the atomic scale, Phys. Rev. Lett. 112 (2014) 136601, https://doi.org/10.1103/PhysRevLett.112.136601.

[59] M. Rosić, D. Zagorac, D. Milivojević, N. Paunović, J. Zagorac, Z. Dohčević-Mitrović, B. Matović, Theoretical and experimental study of octahedral tilting of $Ca_{1-x}Gd_xMnO_3$ ($x = 0.05, 0.1, 0.15, 0.2$) nanometric powders, J. Alloys Compd. 678 (2016) 219–227, https://doi.org/10.1016/j.jallcom.2016.03.173.

[60] A. Dutta, N. Gayathri, R. Ranganathan, Effect of particle size on the magnetic and transport properties of $La_{0.875}Sr_{0.125}MnO_3$, Phys. Rev. B 68 (2003) 54432, https://doi.org/10.1103/PhysRevB.68.054432.

[61] E.T. Swartz, R.O. Pohl, Thermal boundary resistance, Rev. Mod. Phys. 61 (1989) 605–668, https://doi.org/10.1103/RevModPhys.61.605.

[62] C.-W. Nan, R. Birringer, Determining the Kapitza resistance and the thermal conductivity of polycrystals: a simple model, Phys. Rev. B 57 (1998) 8264–8268, https://doi.org/10.1103/PhysRevB.57.8264.

[63] J. Wang, J.K. Carson, M.F. North, D.J. Cleland, A new approach to modelling the effective thermal conductivity of heterogeneous materials, Int. J. Heat Mass Tran. 49 (2006) 3075–3083, https://doi.org/10.1016/j.ijheatmasstransfer.2006.02.007.

[64] J.L. Mi, T.J. Zhu, X.B. Zhao, J. Ma, Nanostructuring and thermoelectric properties of bulk skutterudite compound $CoSb_3$, J. Appl. Phys. 101 (2007) 54314, https://doi.org/10.1063/1.2436927.

[65] M. Gunes, M. Ozenbas, Effect of grain size and porosity on phonon scattering enhancement of $Ca_3Co_4O_9$, J. Alloys Compd. 626 (2015) 360–367, https://doi.org/10.1016/j.jallcom.2014.12.004.

[66] F.P. Zhang, Q.M. Lu, X. Zhang, J.X. Zhang, First principle investigation of electronic structure of $CaMnO_3$ thermoelectric compound oxide, J. Alloys Compd. 509 (2011) 542–545, https://doi.org/10.1016/j.jallcom.2010.09.102.

[67] X. Song, S.A. Paredes Navia, L. Liang, C. Boyle, C.-O. Romo-De-La-Cruz, B. Jackson, A. Hinerman, M. Wilt, J. Prucz, Y. Chen, Grain boundary phase segregation for dramatic improvement of the thermoelectric performance of oxide ceramics, ACS Appl. Mater. Interfaces 10 (2018) 39018–39024, https://doi.org/10.1021/acsami.8b12710.